Nanoscale

Accepted Manuscript

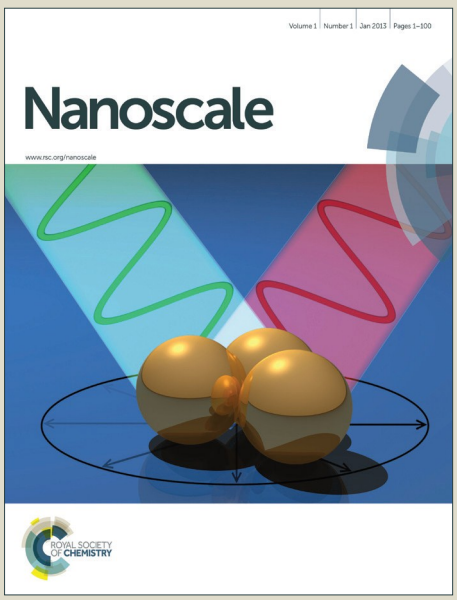

ROYAL SOCIETY OF CHEMISTRY

www.rsc.org/nanoscale

A simple route to diverse noble metal-decorated iron oxide nanoparticles for catalysis

Joan M. Walker and Jeffrey M. Zaleski*

Department of Chemistry, Indiana University, Bloomington, IN

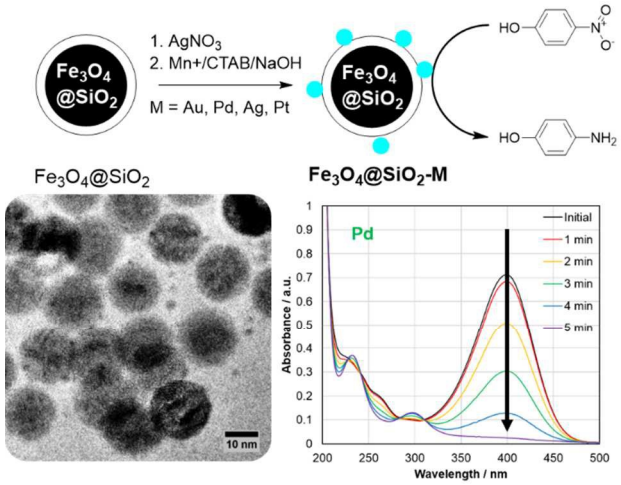

*zaleski@indiana.edu

ABSTRACT

Developing facile synthetic routes to multifunctional nanoparticles combining the magnetic properties of iron oxides with the optical and catalytic utility of noble metal particles remains an important goal in realizing the potential of hybrid nanomaterials. To this end, we have developed a single route to noble metal-decorated magnetic nanoparticles (Fe_3O_4@SiO_2-M; M = Au, Pd, Ag, and PtAg) and characterized them by HRTEM and STEM/EDX imaging to reveal their nanometer size (16 nm Fe_3O_4 and 1-5 nm M seeds) and uniformity. This represents one of the few examples of genuine multifunctional particles on the nanoscale. We show that these hybrid structures have excellent catalytic activity for the reduction of 4-nitrophenol (k_{norm} = 2×10^7 $s^{-1}mol(Pd)^{-1}$; 5×10^6 $s^{-1}mol(Au)^{-1}$; 5×10^5 $s^{-1}mol(PtAg)^{-1}$; 7×10^5 $s^{-1}mol(Ag)^{-1}$). These rates

are the highest reported for nano-sized comparables, and are competitive with mesoparticles of similar composition. Due to their magnetic response, the particles are also suitable for magnetic recovery and maintain >99% conversion for at least four cycles. Using this synthetic route, Fe_3O_4@SiO_2-M particles show great promise for further development as a precursor to complicated anisotropic materials or for applications ranging from nanocatalysis to biomedical sensing.

INTRODUCTION

Multifunctional nanoparticles are fast superseding their single-component analogues in research interest because they have the potential to combine the unique properties of two or more nanomaterials in one entity. This concept has led to advances in biomedical technologies, for example in the development of dual-action theranostics,[1, 2] and holds promise for "green" solutions for improved catalysis and solar energy utilization.[3] However, synthetic control of hybrid materials is quite challenging, and requires a methodology more typical of multistep organic synthesis. Since one must ensure that the preparative conditions for one material do not harm or interfere with the properties of the second material, typical protocols to build these hybrid systems can be tedious, time-consuming, and specific to a single system under study.

Magnetic iron oxide phases, such as magnetite (Fe_3O_4) and maghemite (γ-Fe_2O_3), are particularly attractive as components of multifunctional nanomaterials because they interact with external fields, lending them the ability to be easily recovered and reused or otherwise manipulated by magnetic means. Iron oxide nanoparticles can be readily synthesized by thermal decomposition,[4] co-precipitation,[5] and solvothermal methods,[6] and many reviews have covered the relative strengths of each approach.[7-9] By decorating iron oxide nanoparticles with metallic Au, Ag, Pt,

and Pd ornaments, unique optical and catalytic properties are engendered in multifunctional magnetic-noble metal hybrid materials at the nanoscale. As the synthetic conditions for these constituent materials are generally quite different, most routes propose to either combine two sets of pre-synthesized particles, or decorate the magnetic particle by reducing metal salt precursors *in situ*. The most common magnetic-metallic hybrids take the form of iron oxide mesoparticles (100 nm to 1 micron in diameter) coated with carbon or thick silica layers, upon which reside clusters of metallic nanoparticles.[10-25] While sufficient for their intended purposes, devising additional synthetic strategies for true nanomaterials (< 100 nm diameter) that combine magnetic and noble metal particles remains a meaningful challenge, and examples of such systems in the literature are few.[26-32]

One burgeoning application for noble metal-decorated magnetic nanoparticles is in the field of catalysis, where their magnetic recoverability represents an advantage over other types of heterogeneous catalysts that must be isolated by filtration or centrifugation for reuse.[33-35] To benchmark the suitability of nanoparticles for such applications, it is common to test them for catalytic activity using the reduction of 4-nitrophenol (4-NP) by sodium borohydride in aqueous solution, as monitored by optical spectroscopy.[36] Not only is this a very well-known and understood model reaction, but it also represents a real world necessity, as 4-NP is a common pollutant in wastewater streams and the reduced product, 4-aminophenol, is a useful compound.[37, 38] This reaction falls under the general category of transforming nitroaromatics into functionalized anilines, which is of significant industrial utility. In aqueous solution, sodium borohydride is a sufficiently strong reductant for aromatic nitro groups, but the basal reaction is kinetically quite slow. However, in the presence of many metals, this rate is drastically increased

due to the availability of surface reaction sites.[39] The currently accepted catalytic mechanism can be described by the Langmuir-Hinshelwood model, in which the metal surface facilitates atom and electron transfer between adsorbed 4-NP and hydride to form the hydrogenated product.[40] Ag, Au, Pt, and Pd are all known to be catalytically active for this reaction.[37]

With an eye towards materials suitable for nanocatalysis, we report here a simple, facile route to prepare noble metal-seed decorated iron oxide nanoparticles *via* an *in situ* reduction method under mild conditions. This strategy is effective in producing Pd, Au, and Ag single-metal particles and PtAg bimetallic particles as surface decorations on magnetite (Fe_3O_4) cores that then show catalytic activity toward 4-NP reduction. Overall, these nanoparticles represent a convenient synthetic approach to multifunctional hybrid nanomaterials for wide-ranging potential applications.

RESULTS AND DISCUSSION

SYNTHESIS OF SEED-DECORATED MAGNETIC NANOPARTICLES

The synthesis of seed decorated iron oxide nanoparticles (**Scheme 1**) begins with the preparation of high-quality magnetic cores. Following the classic method of Park *et al.*,[4] monodisperse Fe_3O_4 nanoparticles are synthesized through the thermal decomposition of iron(III) oleate and assessed by TEM, XRD, and SQUID (**Figure 1**). Based on measured TEM sizes, the nanoparticles are 16 ± 1.1 nm in diameter with a narrow size distribution (**Figure 1a**). The iron oxide phase is examined by X-ray diffraction, here indicating magnetite (Fe_3O_4) as the majority phase (**Figure 1b**). The magnetic properties were measured by SQUID, which reveals that they are superparamagnetic at 300 K, meaning that they do not possess remanant magnetism upon the removal of external field (**Figure 1c**). Their magnetization at high field (50 emu/g at 20 kOe) is

modest and fails to fully saturate, typical of iron oxides synthesized from metal oleate precursors.[41]

Simple trialkoxy silane groups were used as facile ligand exchange agents to render the nanoparticles water soluble after surface coordination.[42] The organic-soluble Fe_3O_4-OA were diluted to 1 mg/mL in hexanes, and appropriate amounts of APTMS and MPTMS were added in a 4:1 molar ratio. The amounts used were optimized for nanoparticles of 16 nm diameter; however, the relative amounts of siloxane can easily be adjusted by the surface area-to-volume ratio to accommodate nanoparticles of different diameters. Upon successful surface coating, the nanoparticles precipitate, allowing for a straightforward magnetic collection. After washing with ethanol to remove any excess silanes and oleate, the Fe_3O_4@SiO_2 nanoparticles are solubilized by sonication in dilute acid (CH_3COOH, pH = 3) to form a stable black sol. TEM and DLS analyses reveal that the iron oxides are well-dispersed and coated with a very thin silane layer, which is not directly visible by electron microscopy, although its thickness can be inferred from the measured gap between close packed particles to be 0.6 ± 0.1 nm (**Figure S1a**). The narrow size distribution of non-aggregated particles is confirmed in the DLS data (**Figure S1b**), exhibiting a hydrodynamic diameter of 37 nm, indicative of the nanoparticle core plus siloxane coating and associated protonated amine and solvent layers.[43] Additionally, STEM/EDX mapping was able to distinguish a thin Si-containing layer located around the iron oxide cores, signaling a successful coating step (**Figure S2**).

A mixture of amine- and thiol-terminated siloxanes was utilized in order to confer water solubility (*via* protonation of the amines in acidic solution) and provide isolated sites for metal

coordination *via* the thiol. A solution of silver nitrate is added to the nanoparticle stock and incubated for 30 minutes to allow the silver ions to locate at the nanoparticle surface, presumably through thiol association. Subsequently all silver is reduced *in situ* with sodium borohydride.[23, 44] The small amount of silver is dispersed over all available thiol nucleation sites on the iron oxide surface, meaning that the Ag content is not visible by HRTEM (**Figure 2a**). However, the existence of small silver islands is indicated by EDX spectra taken over a broad area of the sample (**Figure 2b**). Additionally, by increasing the amount of silver nitrate solution added in this step fivefold, small Ag seeds are visible in TEM (**Figure S3a**). Alternatively, by holding the amount of Ag constant, the size of metal sites can be controlled through the thiol to amine ratio. By reducing the relative amount of MPTMS used in the coating step, the Ag was isolated to a smaller area on the nanoparticle surface and small particles are again visible (**Figure S3b**). This reinforces the fact that the thiol is important in determining the silver coordination.

The surface silver sites act as directing agents for the overgrowth of Au, Pd, Pt or additional Ag in the presence of CTAB under basic conditions. Metal seeds closely associated with the iron oxide core surface are visible with a high degree of regularity across the majority of the sample in TEM, and detailed HRTEM images show seeds of narrow size distribution: 2.3 ± 1.2 (Au), 2.0 ± 0.78 (Pd), 2.4 ± 1.0 (Pt), 4.4 ± 2.0 nm (Ag) (**Figure 3**). The identity of the metal is confirmed by STEM/EDX. The STEM images clearly emphasize the Z-contrast between the Au, Pd, Pt, and Ag seeds against the much larger, but less bright, iron oxide particles. Associated elemental maps again localize the noble metal to the small seeds (**Figure 4**).

Four metals were used for the seed decoration of iron oxide nanoparticles and serve to illustrate the adaptability of this synthetic approach. By moderately changing conditions, four noble metals were successfully reduced on the iron oxide surface, albeit by slightly different assumed mechanisms. First, for Au and Pd, it is believed that the initial silver layer serves as a sacrificial reductant for the metal deposition at room temperature.[45, 46] By taking elemental spectra over a broad area, we can confirm the presence of Au or Pd at the expense of the underlying Ag in these samples (**Figure 5**). The diagnostic peaks for Ag at 2.98, 3.15, and 22.2 keV are completely absent in the overgrown material for Au and Pd, while new peaks for Au (2.12 keV) or Pd (2.84, 2.99, 21.2 keV) are clearly present. The presence of silver, CTAB, and NaOH are all deemed to be essential for this process to occur. While CTAB/NaOH has been shown to be an effective reducing environment for Au,[47] the Ag content localized to the iron oxide surface was able to direct the placement and enhance the rate of deposition. In fact, control experiments with $HAuCl_4$, CTAB, and NaOH illustrate the benefit of sacrificial Ag seeds in directing this reaction (**Figure S4**). While gold was reduced in the high concentration CTAB environment under basic conditions, the addition of a sub-stoichiometric amount of silver seeds led to the formation of discrete nanoparticles within 2 h. Similarly, for the seed-decorated iron oxides, little to no Au decoration was observed in the absence of Ag (**Figure S5**). The presence of the Au surface plasmon in the optical spectrum between 500 and 600 nm corroborates the reduction and formation of small Au seeds. Additionally, the reduction proved to be insensitive to the metal salt used; we obtained similar results for $AuBr_3$ and $Pd(NO_3)_2$, reinforcing the wide applicability of this method.

For the two other noble metals used here, Pt and Ag, slightly elevated temperatures are required for successful deposition, presumably due to their lower reduction potentials at room temperature. In the case of Ag, it is assumed that Ag growth occurs on the sites of silver association from the first step. We also believe that the elevated temperatures are sufficient to rearrange the deposited silver, resulting in slightly larger isolated seeds seen decorating the iron oxide nanoparticles. Heating the "Ag10" sample at 60 °C for an equivalent period shows that such rearrangement (or seed "ripening") is likely operative (**Figure S6**). These super seeds provide an excellent platform for the *in situ* reduction of Pt. The proposed mechanism is that the Pt^{2+} in solution initially reacts with the Ag^0 on the nanoparticle surface to galvanically replace it, much like in the Au and Pd cases. However, the silver ions thus released subsequently re-reduce under these conditions. The result is primarily bimetallic PtAg particles, confirmed through EDX spectra and site-specific mapping (**Figures 4, 5**). While Pt and Ag are considered immiscible as bulk metals, several groups have reported PtAg alloys and other bimetallic PtAg structures in nanoscale syntheses.[48-53] Considering the current interest in bimetallic and other mixed metal systems,[54] this synthetic route may provide a convenient avenue to explore the utility of various metal decorations. Overall, and in contrast to other methods, this synthesis represents a straightforward, mild, facile means to produce noble metal seed-decorated iron oxide nanoparticles amenable to various metal precursors with the potential for multiple applications.

CATALYTIC ACTIVITY OF SEED-DECORATED MAGNETIC PARTICLES

To evaluate the suitability of the synthesized nanoparticles for magnetically-recoverable catalyst applications, we tested them for catalytic activity using the reaction of 4-NP with sodium borohydride in aqueous solution, monitored by UV-vis spectroscopy. All show good activity for

the reduction of 4-NP, as indicated by the disappearance of its characteristic λ = 400 nm absorbance peak and appearance of two smaller features at 240 and 300 nm of the 4-aminophenol product (**Figure 6**). Little to no reaction is observed in the absence of noble metal-decorated nanoparticles over the timescale of these experiments (< 60 min, **Figure S7**). Kinetic information can be extracted from these data by assuming a pseudo first-order rate expression and monitoring A_{400} over the course of the experiment (**Figure 7**). The apparent rate constant (k_{obs}) is determined from the linear regime of the resultant dataset, and these values have been summarized in **Table 1**.

Current state-of-the-art noble metal catalysts, including those supported on CeO_2,[55] PAMAM dendrimers,[56] TiO_2,[57] carbon,[58] and spherical polyelectrolyte brushes,[31, 59-62] routinely perform with rate constants upwards of $k_{obs} = 10^{-1}$ s^{-1}. However, within the context of magnetically-recoverable catalysts, our calculated rate constants are in excellent agreement with or exceed literature values for magnetically-recoverable catalysts incorporating noble metal surfaces (**Table S1**).[14, 16, 17, 21, 23, 63] These comparisons are more easily evaluated if the k_{obs} is normalized to the total amount of noble metal present in the sample, in this case determined from the synthetic parameters. Of the sparse examples of truly nano-sized composites, our Fe_3O_4@SiO_2-Au represents the highest normalized rate for a material of this type (*cf.* gold-decorated amine-functionalized magnetite by Zhang *et al.*, $k_{norm} = 2 \times 10^4$ at 2.3 mol% catalyst loading).[32] Furthermore, for noble-metal decorated magnetic mesoparticles, our rates are competitive with some of the best reported for Au (*e.g.* Fe_3O_4@poly(4-vinylpyridine-co-divinylbenzene)@Au by Guo *et al.*, $k_{norm} = 2 \times 10^6$ at 3.9 mol%),[14] Ag (*e.g.* carboxyl-functionalized polymer-coated Fe_3O_4 by Zhou *et al.*, $k_{norm} = 5 \times 10^3$ at 1.3 mol%),[23] and Pd (*e.g.* Pd/Fe_3O_4@SiO_2@m-SiO_2 by

Liu *et al.*, $k_{norm} = 1.5 \times 10^6$ at 1.0 mol%, which were also shown to be effective in hydro-dechlorination reactions).[17]

The morphological similarity between the synthesized Fe_3O_4@SiO_2-M samples allows for interesting comparisons to be made in interpreting their kinetic traces. Of note are two correlated trends: reaction rate and length of induction period.[64] During the induction period, no reaction occurs, as time is required for the reactants to bind to and rearrange the metal surface for it to become active.[65] For the metal seeds studied here, the induction period trends as Pd << Au < PtAg < Ag. Similarly, once the reaction begins, the normalized rates (**Table 1**) span two orders of magnitude from Pd (10^7) to Ag (10^5). These trends are presumably influenced by the same set of factors dealing with the metal surface: substrate binding affinity and geometry; and availability of surface reaction sites. It has recently been shown that surfactant adsorption can profoundly influence the rate of nanocatalysis by presenting a favorable orientation and density of surface sites to incoming reagents.[66] CTAB has been shown in simulation to adopt a flat packing orientation on Au[111] surfaces, where the long flexible alkyl tail nestles among the surface atoms.[67] Differences between the atomic spacings for catalytic surfaces will impact the conformation of adsorbed CTAB and, thus, could preference certain metals for favorable 4-NP reduction. Moreover, different metals show different propensities for hydrogenation reactions based on their abilities to store surface hydrogen species.[37] It is well known that Pd is excellent in this regard, which contributes to its very fast catalytic turnover.[68]

It bears mentioning that of the four catalysts studied here, the Ag sample shows somewhat more complicated behavior. There is a slow catalyst initiation phase followed by a faster, normal

pseudo first-order process, from which the reported rate constant was determined. Such biphasic catalytic activity has also been observed for some Au-containing materials,[19] which is attributed to a competition between adsorption and reduction in the early stages of the reaction. Detailed kinetic analysis of 4-NP reduction on metal nanoparticles indicates that some time is required before the system reaches a stationary state, in which the concentration of surface species is essentially constant, and for the rate limiting step (*i.e.* production of 4-aminophenol) to be established.[39, 65] While the surface transformations involved in nanocatalysis are somewhat complicated,[69] using a general synthetic method allows for the isolation of metal identity as it influences the kinetics of reaction.

Magnetic recoverability was assessed by collecting the dispersed nanoparticles from the solution with a strong permanent magnet and adding fresh reagents. The nanoparticles retain their catalytic activity for three further cycles, albeit with decreased rates over time (**Figure 8**).[70] There are two likely reasons for the decrease in rate apart from the catalyst surface poisoning that is commonly seen in heterogeneous catalysts.[71] First, some separate or weakly-associated non-magnetic noble metal particles may be present and, hence, washed away after the first cycle. This seems to be most likely operative in the Pd case, as the rate drops precipitously between the first and second cycles. Second, the nanoparticles tend to aggregate during magnetic collection due to the basic conditions of this particular model reaction, which reduces the available reactive surface area. Noble metal leaching, a third possible explanation for the decrease in rate, was independently ruled out by centrifuging the reaction mixture after one catalytic cycle. No further reaction was observed when the supernatant was mixed with fresh catalysis reagents. Thus, the mechanism is believed to be heterogeneous with minimal contribution from leached noble metal

ions. The high activity and synthetic ease of Fe_3O_4@SiO_2-M indicate that they have potential utility in the field of nanocatalysis.

CONCLUSION

We have successfully synthesized noble metal seed-decorated iron oxide nanoparticles using four different metal precursors and have fully characterized them by TEM, HRTEM, and STEM/EDX. We have found no other reported method using four different metals by essentially the same technique. Moreover, the synthesized material represents a rare example of a truly nano-sized hybrid, in contrast to many reported syntheses that generate microspheres comprised of nano-sized components. By testing our Fe_3O_4@SiO_2-M particles for their catalytic activity for 4-NP reduction, we find that they meet or exceed normalized rates of other literature examples, with moderate catalyst loading. Additionally, the mild synthetic route represents a versatile springboard that may be amenable to a variety of other metal precursors and substrates (*e.g.* glass, see Supplementary Information[70]). The seed decorated products themselves could also have utility outside of nanocatalysts, for example as multifunctional sensor components or as synthetic precursors to higher order hybrid and anisotropic nanomaterials.

ACKNOWLEDGEMENTS

The authors would like to acknowledge the excellent assistance of Dr. David Morgan (Indiana University Electron Microscopy Center) in collecting the HRTEM/STEM/EDX data. SQUID data was collected with the assistance of Radian Wang (IU Physics Dept.), and XRD data by the Indiana University Molecular Structure Center (NSF Grant # CHE-1048613). The financial support of the National Science Foundation (NSF Grant # CHE-1265703) is also gratefully acknowledged.

Materials and Physical Methods. All chemicals and solvents were purchased from commercial sources and used as received. Millipore or 18 MΩ H_2O was used for all aqueous preparations. Dynamic light scattering (DLS) measurements were acquired on a Zetasizer Nano ZS equipped with a $\lambda = 633$ nm source. SQUID measurements were performed on a Quantum Design MMPS on solid state samples. X-ray powder diffraction (XRD) patterns were acquired on a PANalytical Empyrean instrument with Cu Kα radiation. Transmission electron microscopy (TEM) was performed using a JEOL 1010 microscope operating at 80 kV. HRTEM, STEM, and EDX data were collected on a JEOL JEM 3200FS at 300 kV accelerating voltage.

Synthesis of Fe_3O_4-OA. Organic soluble iron oxide nanoparticles were synthesized *via* the high temperature decomposition route of Park *et al*.[4] Fe(III)oleate was prepared by vigorously stirring $FeCl_3 \cdot 6H_2O$ (1.0 g, 3.7 mmol) with sodium oleate (3.0 g, 9.9 mmol) overnight at RT in a mixed solvent system (6 mL H_2O, 8 mL EtOH, 14 mL hexanes), isolated by extraction into hexanes, and stored as a stock solution (0.2 g/mL) in octadecene at -20 °C. After thoroughly degassing 5 mL of the stock precursor solution under vacuum at 90 °C for 90 min, it was heated to reflux at 5 °C/min. Refluxing at 310 °C for 12 min rendered a black solution, which was cooled under N_2. The resultant nanoparticles were isolated by 3 precipitation-centrifugation cycles in hexanes/isopropanol (1:7) and stored as a stock solution (5 mg/mL) in hexanes or $CHCl_3$.

Preparation of Fe_3O_4@SiO_2. Fe_3O_4-OA (15 mL hexane solution, 1 mg/mL) was stirred overnight with 4 μL (3-mercaptopropyl)trimethoxysilane (2.15×10^{-5} mol, MPTMS) and 15 μL (3-aminopropyl)trimethoxysilane (8.59×10^{-5} mol, APTMS). The black precipitate was collected with a permanent magnet to allow the hexane supernatant to be decanted. The solid

was then washed twice with ethanol (5 mL), once with H_2O (5 mL), and finally reconstituted in 3 mL dilute acetic acid (pH = 3) with sonication to render a stable dark brown solution.

Seed decoration of Fe_3O_4@SiO_2. To 100 μL aliquots of Fe_3O_4@SiO_2 was added 10 μL of $AgNO_3$ (10 mM). After 30 min, 25 μL of ice-cold $NaBH_4$ (10 mM) was added and incubated for 60 min. The reduced samples were centrifuged (10000 rpm × 10 min) and reconstituted in 100 μL H_2O. These samples are indicated as Fe_3O_4@SiO_2-Ag10. Seed growth could be accomplished by using the Ag deposits as a sacrificial reductant and/or nucleation site for the overgrowth of Au, Pd, Pt, or additional Ag. A growth solution of equal parts CTAB (0.1 M) and 0.4 mM metal salt solution ($HAuCl_4$, $PdCl_2$/2HCl, K_2PtCl_4, or $AgNO_3$) was added, followed by the addition of NaOH (1 M). Seed nucleation for Au and Pd was controlled by the iterative addition of 50 μL of the growth solution and 5 μL of base at 2 h intervals at RT. For Pt and Ag, a single 150 μL aliquot of growth solution was added with 15 μL NaOH, and the solution incubated at 60 °C for 6 h. Excess reagents were removed by centrifugation (10000 rpm × 10 min), and the decorated nanoparticles were readily reconstituted in 100 μL H_2O.

Reduction of 4-nitrophenol. A stock solution was prepared by mixing 450 μL 4-nitrophenol (4-NP, 1 mM), 4.5 mL (20 mM) $NaBH_4$, and 10 mL H_2O. For each nanoparticle sample, 1 mL of the stock solution was placed in a quartz cuvette and 2.5 μL Fe_3O_4@SiO_2-M was added. The absorption spectrum was then monitored with an Agilent Cary 8454 spectrophotometer at 30 s intervals. For magnetic recoverability trials, the nanoparticles were collected after completion of the reaction *via* a N48-grade neodymium magnet (1/2″ dia. × 1/4″) and resuspended in fresh catalysis solution.

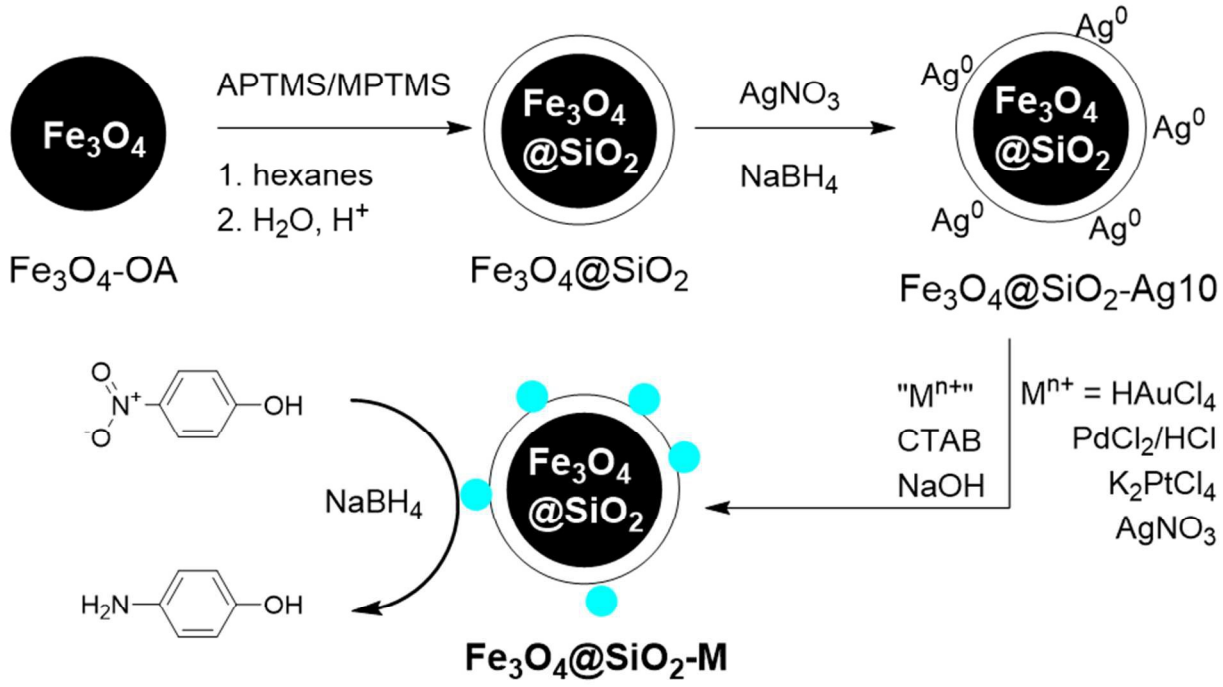

Scheme 1. Stepwise synthesis of Fe_3O_4@SiO_2-M (M = Au, Pd, Ag, or PtAg), which are then used for the reduction of 4-NP to 4-aminophenol.

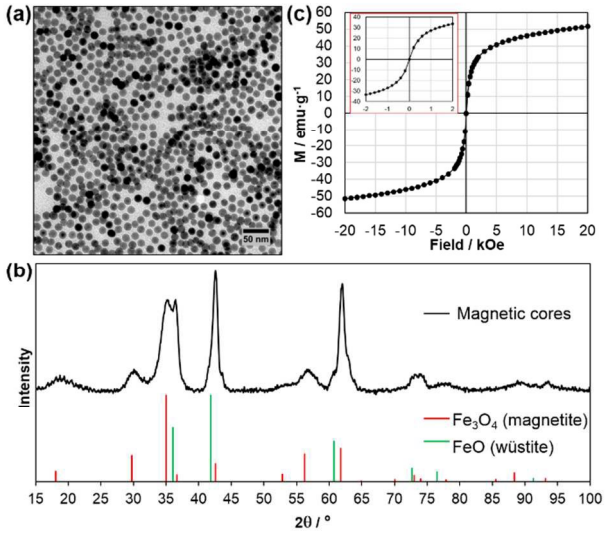

Figure 1. (a) TEM image of the monodisperse IONP cores with diameter 16.1 +/- 1.1 nm. (b) The powder diffraction pattern of the inorganic nanoparticle cores indexes to Fe_3O_4 (magnetite, PDF 01-079-0416, line spectrum shown in red), broadened because of their small size, with some FeO (wüstite, PDF 01-073-2144, shown in green) component. (c) Magnetization curve for the core material, taken at 300 K. The absence of hysteresis (inset) shows that the nanoparticles are superparamagnetic.

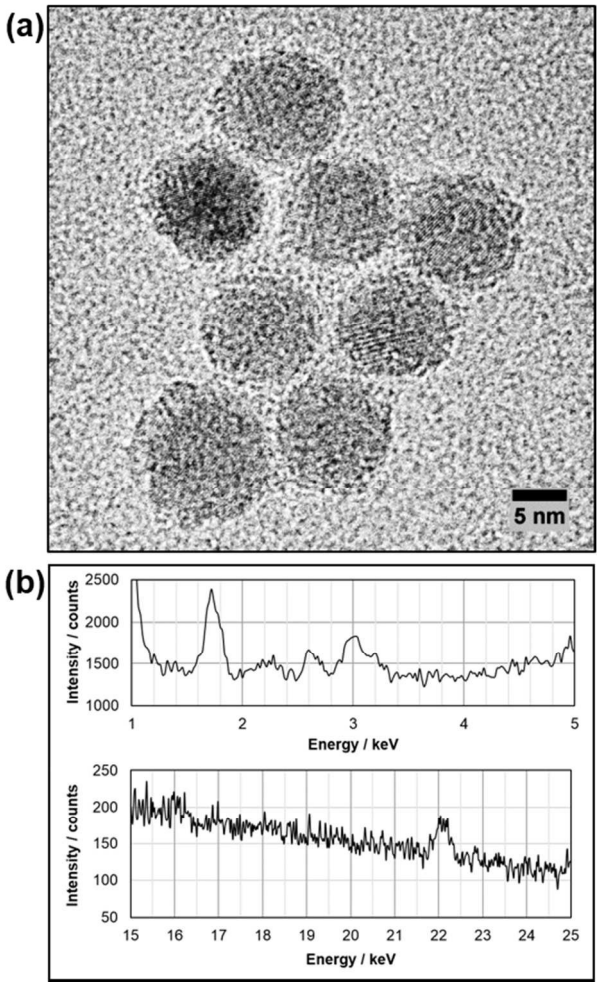

Figure 2. Silver is used as an intermediate growth director in the synthesis of seed-decorated iron oxides. (a) The Ag used is distributed very finely over the entire sample, preventing the imaging of silver particles in HRTEM; (b) however, the presence of Ag in this material is confirmed by the peaks at 3 and 22 keV in the EDX spectra.

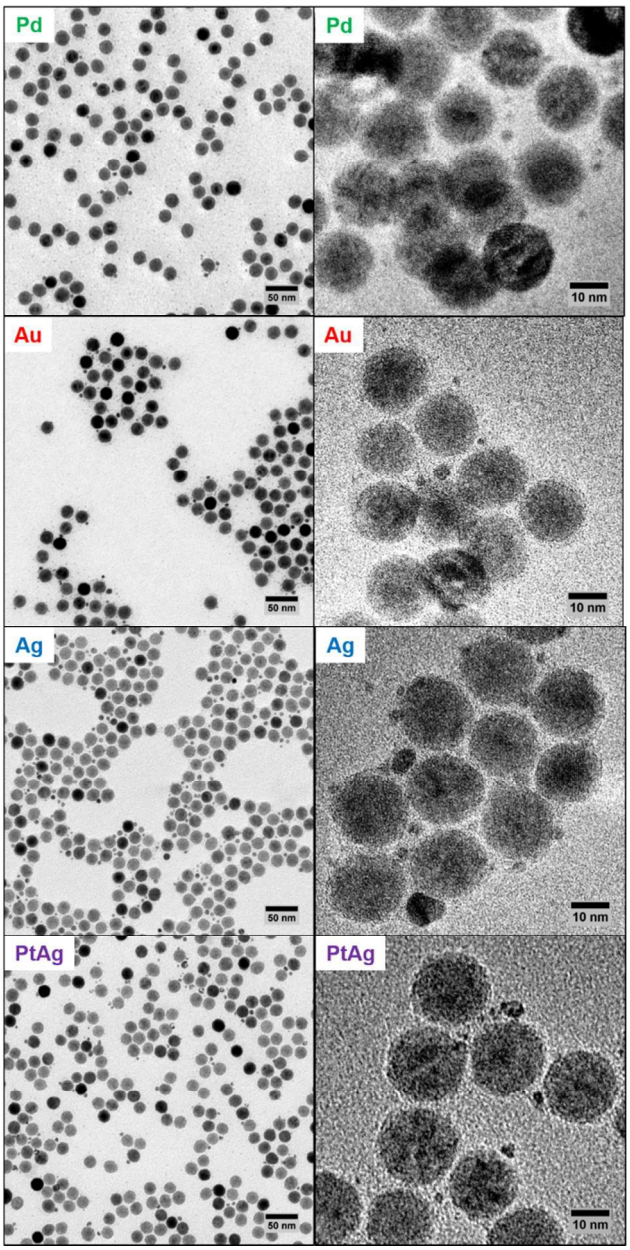

Figure 3. The seed-decorated Fe_3O_4 nanoparticles have an excellent distribution of noble metal seeds over the majority of the sample, as shown in the widefield TEM views in the left column. HRTEM imaging reveals more detail of the core crystallinity and small seeds ranging in size from 1-to-5 nm (right column).

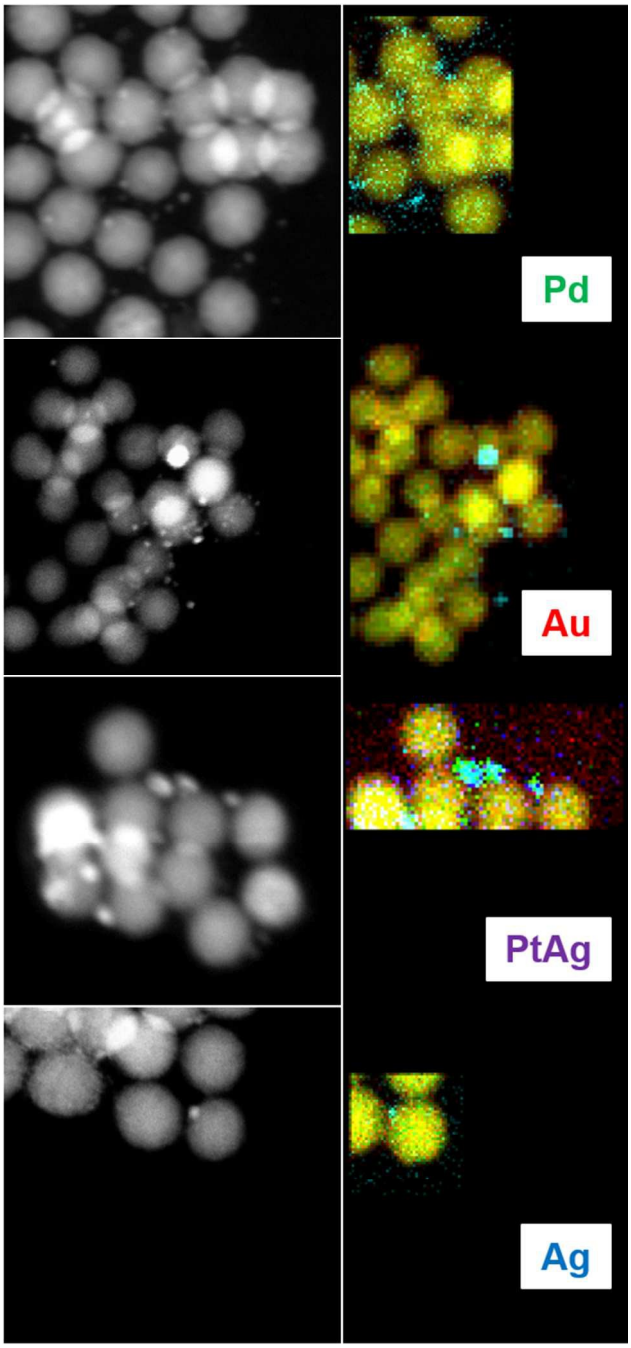

Figure 4. The elemental identity of the seed-decorated IONPs was investigated with STEM/EDX mapping. For each map, Fe is shown in green and O in red; thus, their colocalization is indicated by the yellow hue of the core nanoparticles. For Pd, Au, and Ag, the noble metal is mapped in cyan. For the PtAg sample, Pt is mapped in green and Ag in blue, resulting in a cyan coloration of alloyed particles.

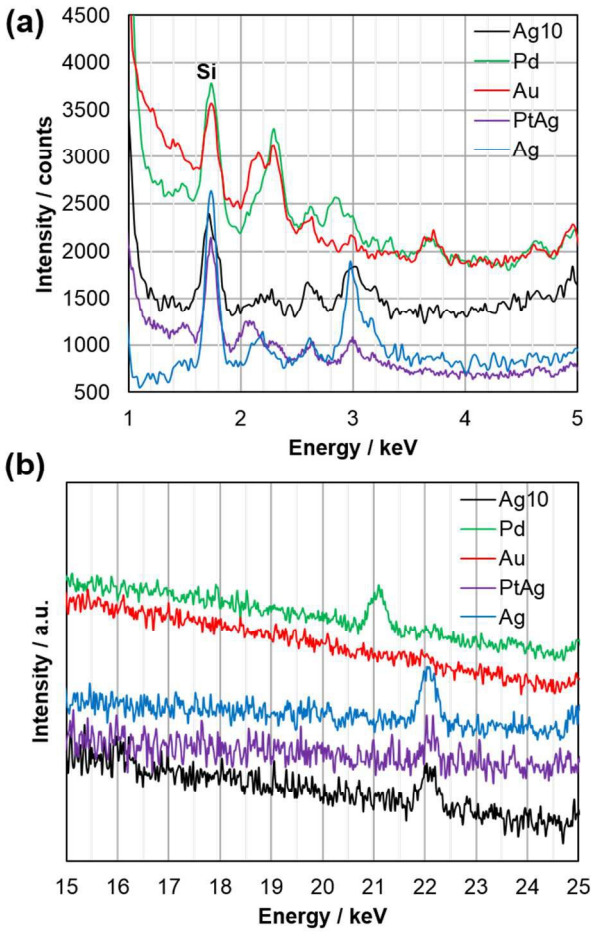

Figure 5. EDX spectra of the seed decorated iron oxide samples show the presence of the noble metals in the samples with key peaks in the low (a) and high (b) energy ranges: 2.05 (Pt, Mα); 2.12 (Au, Mα); 2.98 (Ag, Lα); 21.2 (Pd, Kα); 22.2 (Ag, Kα). Importantly, the spectra for Pd and Au samples contain no Ag, indicating that the initial silver content is completely consumed by galvanic replacement. *n.b.* Spectra in (b) have been offset for comparison.

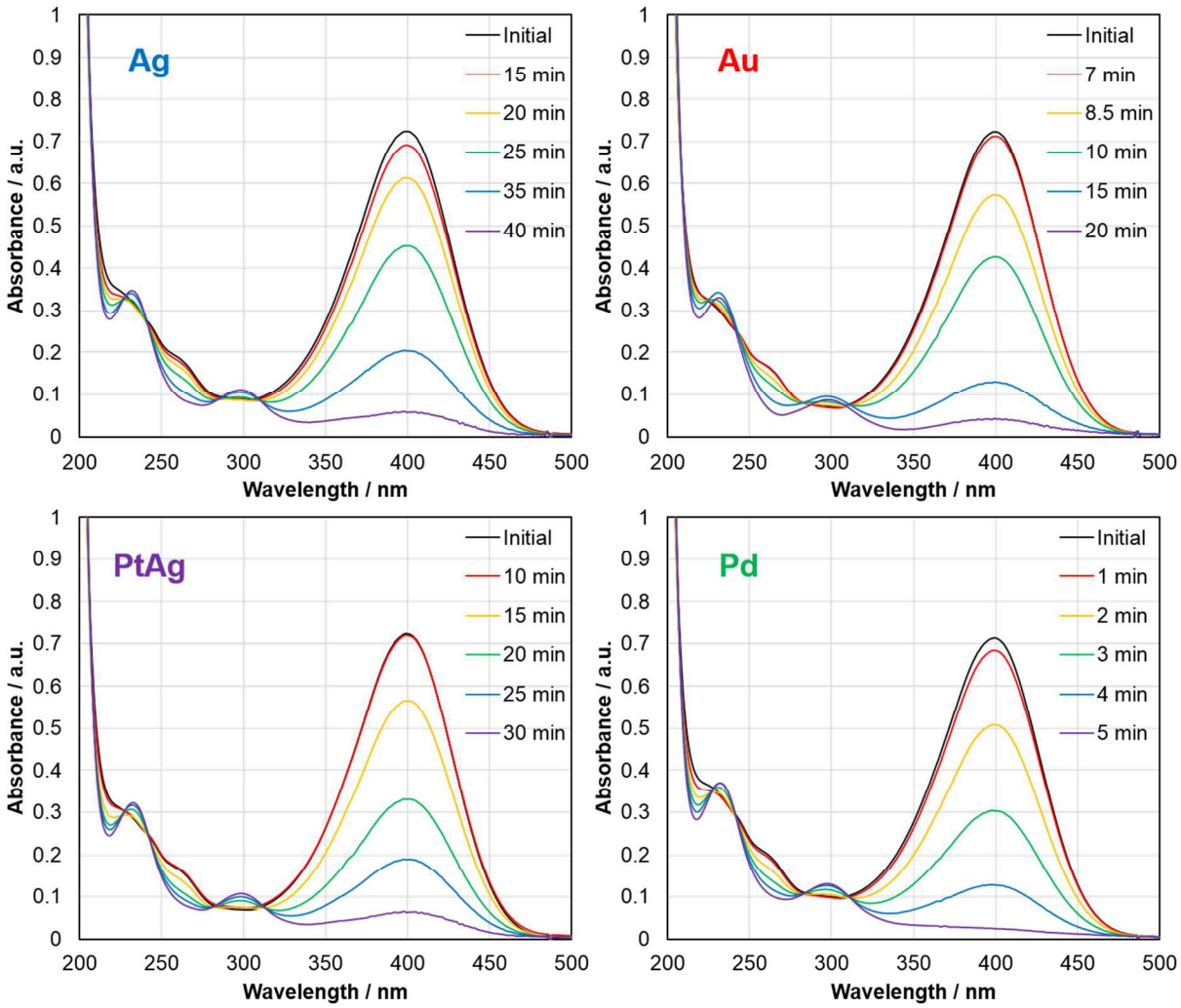

Figure 6. The catalytic reduction of 4-NP by $NaBH_4$ was monitored by UV-vis spectroscopy. While the stock solution (3×10^{-5} M 4-NP; 6×10^{-3} M $NaBH_4$) is stable over the course of the experiment (60 min), the characteristic absorbance of 4-NP at λ = 400 nm rapidly disappears with the addition of seed-decorated Fe_3O_4, with a concomitant growth of two small absorbances at 300 nm and 240 nm of the 4-aminophenol product.

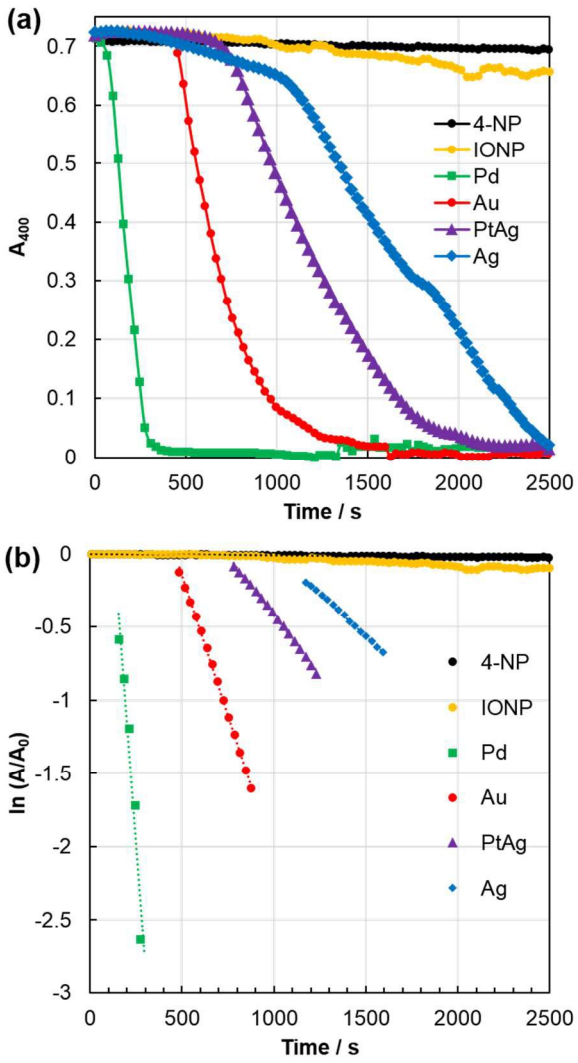

Figure 7. (a) The absorbance of 4-NP at 400 nm was monitored over time in order to determine the kinetics of the catalytic reduction. The data become noisy after the 4-NP has been completely consumed as the $NaBH_4$ continues to react on the nanoparticle surfaces, generating bubbles in the sample solutions. (b) The kinetics of the reduction of 4-NP in the presence of each nanoparticle sample were determined by a first-order rate equation from the linear region of the decay curve.

Sample	k_{obs} / s^{-1}	±	k normalized to M / $s^{-1}mol^{-1}$
4-NP	8.63×10^{-6}		--
Fe_3O_4	5.03×10^{-5}		--
Fe_3O_4-Pd	1.26×10^{-2}	0.24×10^{-2}	1.68×10^{7}
Fe_3O_4-Au	4.41×10^{-3}	0.60×10^{-3}	5.52×10^{6}
Fe_3O_4-PtAg	1.69×10^{-3}	0.35×10^{-3}	5.21×10^{5}
Fe_3O_4-Ag	2.16×10^{-3}	0.94×10^{-3}	6.66×10^{5}

Table 1. Kinetic data for the model reaction in the presence of the various nanoparticle samples. Values reported for Fe_3O_4@SiO_2-M are the average rates of at least three trials. For normalization purposes, the amount of metal was calculated based on synthesis parameters. (*n.b.* M = Pd, Au, Ag, or Pt+Ag; catalyst loading = 2.0 mol% for Au and Pd, 10.8 mol% for PtAg and Ag)

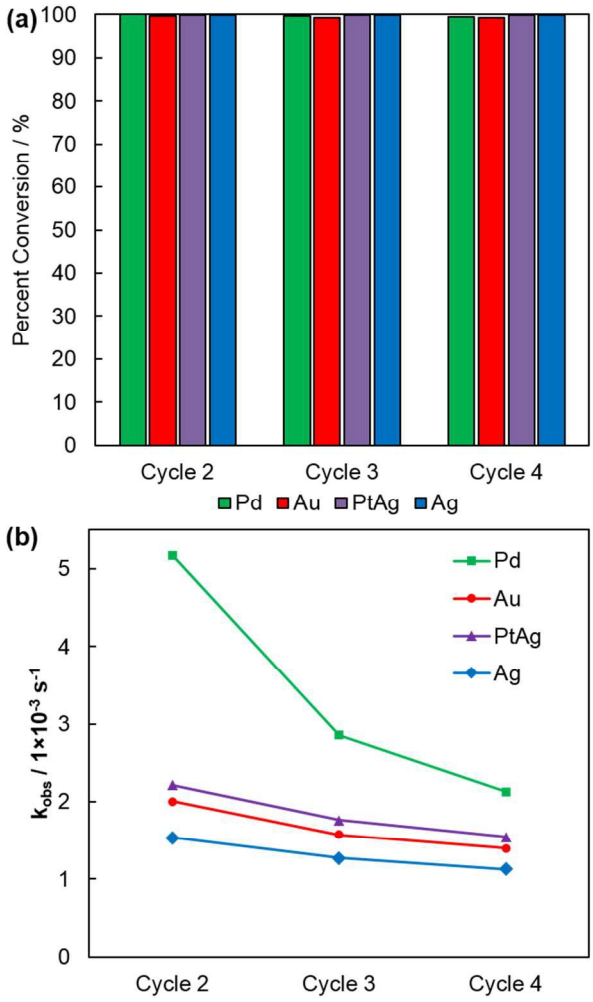

Figure 8. The seed-decorated IONPs are conveniently collected with an external magnet and maintain their catalytic activity for at least three further cycles with (a) excellent product conversion and (b) modest reduction in rate due to catalyst poisoning, etc.

REFERENCES

1. L. K. Bogart, G. Pourroy, C. J. Murphy, V. Puntes, T. Pellegrino, D. Rosenblum, D. Peer and R. Lévy, *ACS Nano*, 2014, **8**, 3107-3122.
2. G. Seeta Rama Raju, L. Benton, E. Pavitra and J. S. Yu, *Chem. Commun.*, 2015, **51**, 13248-13259.
3. S. B. Kalidindi and B. R. Jagirdar, *ChemSusChem*, 2012, **5**, 65-75.
4. J. Park, K. An, Y. Hwang, J.-G. Park, H.-J. Noh, J.-Y. Kim, J.-H. Park, N.-M. Hwang and T. Hyeon, *Nat. Mater.*, 2004, **3**, 891-895.
5. R. Massart, *IEEE Trans. Magn.*, 1981, **MAG-17**, 1247-1248.
6. H. Deng, X. Li, Q. Peng, X. Wang, J. Chen and Y. Li, *Angew. Chem. Int. Ed.*, 2005, **44**, 2782-2785.
7. L. H. Reddy, J. L. Arias, J. Nicolas and P. Couvreur, *Chem. Rev.*, 2012, **112**, 5818-5878.
8. E. Amstad, M. Textor and E. Reimhult, *Nanoscale*, 2011, **3**, 2819-2843.
9. K. Turcheniuk, A. V. Tarasevych, V. P. Kukhar, R. Boukherroub and S. Szunerits, *Nanoscale*, 2013, **5**, 10729-10752.
10. Q. An, M. Yu, Y. Zhang, W. Ma, J. Guo and C. Wang, *J. Phys. Chem. C*, 2012, **116**, 22432-22440.
11. Y. Chi, Q. Yuan, Y. Li, J. Tu, L. Zhao, N. Li and X. Li, *J. Colloid Interface Sci.*, 2012, **383**, 96-102.
12. X. Du, J. He, J. Zhu, L. Sun and S. An, *Appl. Surf. Sci.*, 2012, **258**, 2717-2723.
13. J. Ge, T. Huynh, Y. Hu and Y. Yin, *Nano Lett.*, 2008, **8**, 931-934.
14. W. Guo, Q. Wang, G. Wang, M. Yang, W. Dong and J. Yu, *Chem. - Asian J.*, 2013, **8**, 1160-1167.
15. C. Jin, Y. Wang, H. Wei, H. Tang, X. Liu, T. Lu and J. Wang, *J. Mater. Chem. A*, 2014, **2**, 11202-11208.
16. B. Liu, D. Zhang, J. Wang, C. Chen, X. Yang and C. Li, *J. Phys. Chem. C*, 2013, **117**, 6363-6372.
17. Y. Liu, W. Zhang, X. Li, X. Le and J. Ma, *New J. Chem.*, 2015, **39**, 6474-6481.
18. Z. u. Rahman, Y. Ma, J. Hu, Y. Xu, W. Wang and X. Chen, *RSC Adv.*, 2014, **4**, 5012-5020.
19. M. Rocha, C. Fernandes, C. Pereira, S. L. H. Rebelo, M. F. R. Pereira and C. Freire, *RSC Adv.*, 2015, **5**, 5131-5141.
20. Q. Wang, W. Jia, B. Liu, A. Dong, X. Gong, C. Li, P. Jing, Y. Li, G. Xu and J. Zhang, *J. Mater. Chem. A*, 2013, **1**, 12732-12741.
21. P. Zhang, R. Li, Y. Huang and Q. Chen, *ACS Appl. Mater. Interfaces*, 2014, **6**, 2671-2678.
22. J. Zheng, Y. Dong, W. Wang, Y. Ma, J. Hu, X. Chen and X. Chen, *Nanoscale*, 2013, **5**, 4894-4901.
23. W. Zhou, Y. Zhou, Y. Liang, X. Feng and H. Zhou, *RSC Adv.*, 2015, **5**, 50505-50511.
24. M. Zhu, C. Wang, D. Meng and G. Diao, *J. Mater. Chem. A*, 2013, **1**, 2118-2125.
25. Y. Zhu, J. Shen, K. Zhou, C. Chen, X. Yang and C. Li, *J. Phys. Chem. C*, 2011, **115**, 1614-1619.
26. M. Abbas, S. R. Torati and C. Kim, *Nanoscale*, 2015, **7**, 12192-12204.
27. S.-W. Cao, J. Fang, M. M. Shahjamali, Z. Wang, Z. Yin, Y. Yang, F. Y. C. Boey, J. Barber, S. C. J. Loo and C. Xue, *CrystEngComm*, 2012, **14**, 7229-7235.

28. K. Jiang, H.-X. Zhang, Y.-Y. Yang, R. Mothes, H. Lang and W.-B. Cai, *Chem. Commun.*, 2011, **47**, 11924-11926.
29. F.-H. Lin and R.-A. Doong, *Appl. Catal., A*, 2014, **486**, 32-41.
30. S. Su, G. Yue, D. Huang, G. Yang, X. Lai and P. Zhao, *RSC Adv.*, 2015, **5**, 44018-44021.
31. S. Wu, J. Kaiser, X. Guo, L. Li, Y. Lu and M. Ballauff, *Ind. Eng. Chem. Res.*, 2012, **51**, 5608-5614.
32. F. Zhang, N. Liu, P. Zhao, J. Sun, P. Wang, W. Ding, J. Liu, J. Jin and J. Ma, *Appl. Surf. Sci.*, 2012, **263**, 471-475.
33. T. Cheng, D. Zhang, H. Li and G. Liu, *Green Chem.*, 2014, **16**, 3401-3427.
34. D. Wang and D. Astruc, *Chem. Rev.*, 2014, **114**, 6949-6985.
35. D. Zhang, C. Zhou, Z. Sun, L.-Z. Wu, C.-H. Tung and T. Zhang, *Nanoscale*, 2012, **4**, 6244-6255.
36. P. Herves, M. Perez-Lorenzo, L. M. Liz-Marzan, J. Dzubiella, Y. Lu and M. Ballauff, *Chem. Soc. Rev.*, 2012, **41**, 5577-5587.
37. P. Zhao, X. Feng, D. Huang, G. Yang and D. Astruc, *Coord. Chem. Rev.*, 2015, **287**, 114-136.
38. H. Hu, J. H. Xin, H. Hu, X. Wang, D. Miao and Y. Liu, *J. Mater. Chem. A*, 2015, **3**, 11157-11182.
39. S. Gu, S. Wunder, Y. Lu, M. Ballauff, R. Fenger, K. Rademann, B. Jaquet and A. Zaccone, *J. Phys. Chem. C*, 2014, **118**, 18618-18625.
40. M. A. Vannice, *Kinetics of Catalytic Reactions*, Springer, 2005.
41. R. Chen, M. G. Christiansen and P. Anikeeva, *ACS Nano*, 2013, **7**, 8990-9000.
42. R. De Palma, S. Peeters, M. J. Van Bael, H. Van den Rul, K. Bonroy, W. Laureyn, J. Mullens, G. Borghs and G. Maes, *Chem. Mater.*, 2007, **19**, 1821-1831.
43. A. P. Herrera, C. Barrera and C. Rinaldi, *J. Mater. Chem.*, 2008, **18**, 3650-3654.
44. Y. Zhang, W. Yan, Z. Sun, X. Li and J. Gao, *RSC Adv.*, 2014, **4**, 38040-38047.
45. S. Bhana, B. K. Rai, S. R. Mishra, Y. Wang and X. Huang, *Nanoscale*, 2012, **4**, 4939-4942.
46. Y.-H. Chien, M.-F. Tsai, V. Shanmugam, K. Sardar, C.-L. Huang and C.-S. Yeh, *Nanoscale*, 2013, **5**, 3863-3871.
47. J. Tang, J. Huang and S.-Q. Man, *Spectrochim. Acta, Part A*, 2013, **103**, 349-355.
48. W. He, X. Wu, J. Liu, K. Zhang, W. Chu, L. Feng, X. Hu, W. Zhou and S. Xie, *Langmuir*, 2010, **26**, 4443-4448.
49. M. R. Kim, D. K. Lee and D.-J. Jang, *Appl. Catal., B*, 2011, **103**, 253-260.
50. Z. Peng and H. Yang, *J. Solid State Chem.*, 2008, **181**, 1546-1551.
51. Z. Peng, H. You and H. Yang, *ACS Nano*, 2010, **4**, 1501-1510.
52. W. Zhang, J. Yang and X. Lu, *ACS Nano*, 2012, **6**, 7397-7405.
53. K. D. Gilroy, P. Farzinpour, A. Sundar, R. A. Hughes and S. Neretina, *Chem. Mater.*, 2014, **26**, 3340-3347.
54. Y. Dai, Y. Wang, B. Liu and Y. Yang, *Small*, 2015, **11**, 268-289.
55. J. Zhang, G. Chen, D. Guay, M. Chaker and D. Ma, *Nanoscale*, 2014, **6**, 2125-2130.
56. J. A. Johnson, J. J. Makis, K. A. Marvin, S. E. Rodenbusch and K. J. Stevenson, *J. Phys. Chem. C*, 2013, **117**, 22644-22651.
57. H. Zhang, X. Li and G. Chen, *J. Mater. Chem.*, 2009, **19**, 8223-8231.
58. T. Ji, L. Chen, M. Schmitz, F. S. Bao and J. Zhu, *Green Chem.*, 2015, **17**, 2515-2523.
59. S. Gu, Y. Lu, J. Kaiser, M. Albrecht and M. Ballauff, *PCCP*, 2015, **17**, 28137-28143.

60. Y. Mei, Y. Lu, F. Polzer, M. Ballauff and M. Drechsler, *Chem. Mater.*, 2007, **19**, 1062-1069.
61. Y. Mei, G. Sharma, Y. Lu, M. Ballauff, M. Drechsler, T. Irrgang and R. Kempe, *Langmuir*, 2005, **21**, 12229-12234.
62. M. Schrinner, F. Polzer, Y. Mei, Y. Lu, B. Haupt, M. Ballauff, A. Göldel, M. Drechsler, J. Preussner and U. Glatzel, *Macromol. Chem. Phys.*, 2007, **208**, 1542-1547.
63. M. An, J. Cui and L. Wang, *J. Phys. Chem. C*, 2014, **118**, 3062-3068.
64. S. Wunder, Y. Lu, M. Albrecht and M. Ballauff, *ACS Catalysis*, 2011, **1**, 908-916.
65. S. Wunder, F. Polzer, Y. Lu, Y. Mei and M. Ballauff, *J. Phys. Chem. C*, 2010, **114**, 8814-8820.
66. R. Coppage, J. M. Slocik, H. Ramezani-Dakhel, N. M. Bedford, H. Heinz, R. R. Naik and M. R. Knecht, *J. Am. Chem. Soc.*, 2013, **135**, 11048-11054.
67. J. Feng, R. B. Pandey, R. J. Berry, B. L. Farmer, R. R. Naik and H. Heinz, *Soft Matter*, 2011, **7**, 2113-2120.
68. J. Durand, E. Teuma and M. Gómez, *Eur. J. Inorg. Chem.*, 2008, **2008**, 3577-3586.
69. S. Zhang, L. Nguyen, Y. Zhu, S. Zhan, C.-K. Tsung and F. Tao, *Acc. Chem. Res.*, 2013, **46**, 1731-1739.
70. An alternative means of recovery is to use nanocatalysts supported on macroscale glass substrates, which can be mechanically removed from solution. The reported *in situ* reduction method is highly effective in producing noble-metal decorated silica (see Supplementary Information for synthetic details). Using glass capillaries coated with either APTMS or MPTMS, the mild *in situ* reducing conditions generated catalytically active substrates decorated with Au, Pd, or Pt. These were compared against glass substrates treated with metal salt and $NaBH_4$ (direct reduction) and those incubated with separately-synthesized seeds (seed attachment). The observed rate constants for the hydrogenation of 4-NP for these assemblies were comparable to those for seed attachment and far exceeded those by direct reduction. The success of this method indicates that the mild conditions used are extremely versatile as a means for generating heterostructures of diverse types.
71. J. A. Widegren and R. G. Finke, *J. Mol. Catal. A: Chem.*, 2003, **198**, 317-341.